Corrosion Science 78 (2014) 121–129

Contents lists available at ScienceDirect

Corrosion Science

journal homepage: www.elsevier.com/locate/corsci

Plasma modified Mg–Nd–Zn–Zr alloy with enhanced surface corrosion resistance

Guosong Wu [a], Xuming Zhang [a], Ying Zhao [a], Jamesh Mohammed Ibrahim [a], Guangyin Yuan [b,*], Paul K. Chu [a,*]

[a] Department of Physics and Materials Science, City University of Hong Kong, Tat Chee Avenue, Kowloon, Hong Kong, China
[b] National Engineering Research Center of Light Alloy Net Forming, Shanghai Jiao Tong University, Shanghai 200240, China

ARTICLE INFO

Article history:
Received 1 April 2013
Accepted 25 September 2013
Available online 2 October 2013

Keywords:
A. Magnesium
B. EIS
B. Polarization
B. Ion implantation
C. Interfaces

ABSTRACT

Plasma immersion ion implantation and deposition (PIII&D) is conducted to modify the corrosion behavior of Mg–Nd–Zn–Zr alloy. A diamond-like carbon film (DLC) with a thickness of about 200 nm is formed on the surface after acetylene PIII&D and the resulting corrosion resistance in the 0.9 wt% NaCl solution is significantly improved. The corrosion mechanism is discussed from the perspective of random defects in the DLC film.

1. Introduction

Compared to steels and aluminum alloys, magnesium alloys have lower strength, poorer ductility, and worse corrosion resistance and so their industrial applications have historically been hampered. Nevertheless, Mg and Mg alloys have several properties that make them attractive to electronics, automobiles, aerospace components, and biomedical implants and devices [1–6]. For instance, their low density bodes well for light-duty transportation vehicles with increased fuel efficiency and reduced emissions [7–10] and the easy recyclability makes them environmentally friendly [11,12]. In addition, the unique biodegradation provides the possibility of avoiding a second surgery when they are used as biomedical implants in bone fracture repair [13–15]. Therefore, it is imperative to improve the properties of Mg and Mg alloys to widen the applications.

Dramatic changes in properties such as wear resistance, corrosion resistance, and biocompatibility can be achieved by deposition of a coating [16–21]. Magnesium is a very active metal in the galvanic series inducing galvanic corrosion when in electrical contact with many other conductive materials in the same electrolyte [22,23]. Defects such as pores and cracks are usually unavoidable in coatings [24,25] and galvanic corrosion occurs when the electrolyte reaches the interface between the coating and substrate *via* these defects. The adhesion between diamond-like carbon (DLC) and Mg can be enhanced by means of a Cr interlayer but the corrosion resistance deteriorates due to the galvanic cells generated in the defects [26]. Al and Ti films as interlayers have also been deposited on magnesium alloy before deposition of AlO_xN_y. Since Al is closer to Mg in the galvanic series, the soft Al film can alleviate the galvanic effect compared to a hard Ti film but at the expense of surface hardness [27]. Ion implantation can increase the bonding strength between the substrate and coating because energetic ion bombardment can create a clean surface prior to deposition [28]. An ion implanted layer can further serve as a barrier to galvanic effects and consequently, nitrogen ion implantation has been conducted on magnesium alloy before Ti deposition. However, the improvement is limited because of the big galvanic difference between Ti and Mg [29].

To facilitate our analysis of the galvanic effect, the galvanic current can be simplified using the following relationship [30]:

$$I = \frac{E_C - E_{Mg}}{R_s + R_{Mg\text{-}C} + R_{p(Mg)} + R_{p(C)}} \quad (1)$$

where E_C is the corrosion potential of the cathode, E_{Mg} is the corrosion potential of the anode, R_s is the electrical resistance of the electrolyte, $R_{Mg\text{-}C}$ is the electrical resistance between the anode and cathode, and $R_{p(Mg)}$ and $R_{p(C)}$ are the polarization resistance of the anode and cathode, respectively. A small galvanic current is generated by increasing R_s, $R_{Mg\text{-}C}$, $R_{p(Mg)}$, and $R_{p(C)}$. Since R_s and $R_{p(Mg)}$ do not change under fixed conditions, larger $R_{Mg\text{-}C}$ and $R_{p(C)}$ should be

* Corresponding authors. Tel.: +86 21 3420 3051; fax: +86 21 3420 2794 (G. Yuan), tel.: +852 3442 7724; fax: +852 3442 0542 (P.K. Chu).
E-mail addresses: gyyuan@sjtu.edu.cn (G. Yuan), paul.chu@cityu.edu.hk (P.K. Chu).

0010-938X/$ - see front matter © 2013 Elsevier Ltd. All rights reserved.
http://dx.doi.org/10.1016/j.corsci.2013.09.007

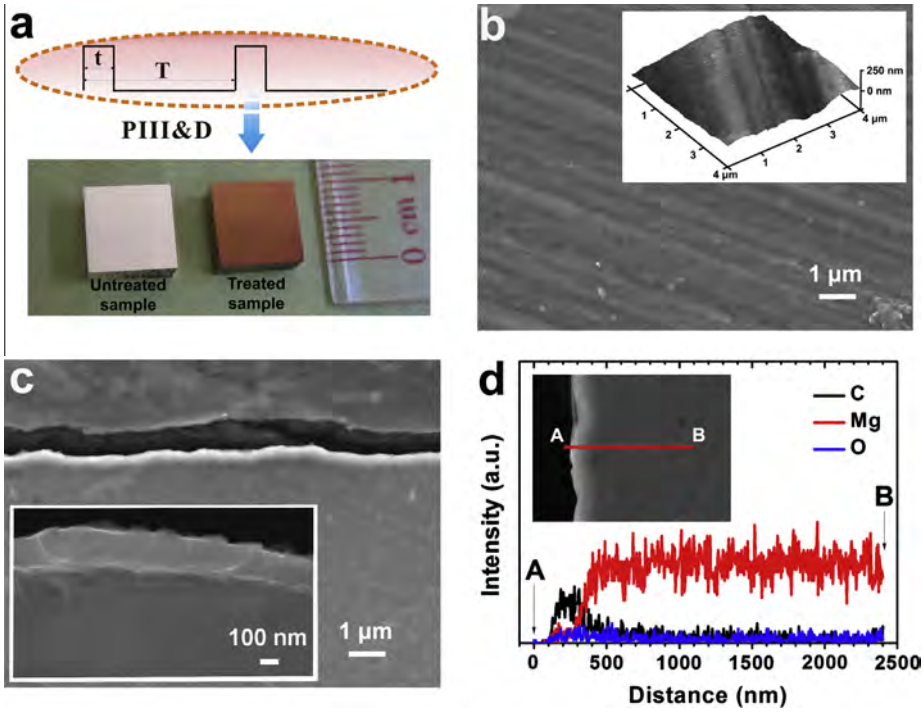

Fig. 1. (a) Surface appearance of the untreated and treated samples. (b) SEM picture of surface morphology of the film with the inset showing the magnified surface obtained by AFM. (c) SEM view of the cross section of the plasma-modified sample with the inset showing a magnified picture of the film. (d) EDS line scan of the film.

considered when selecting the materials and consequently, an insulating and chemically inert coating such as diamond-like carbon (DLC) [25] is preferred.

Plasma immersion ion implantation and deposition (PIII&D) is an advanced surface modification technique combining energetic ion implantation and low-energy plasma deposition. The specimens are surrounded by a plasma and pulse-biased to a high negative potential relative to the chamber wall, making processing of samples with a complex shape convenient [21,30]. Mg–3.0Nd–0.2Zn–0.4Zr (wt%) alloy is a kind of rare earth containing magnesium-based materials with excellent mechanical strength [31,32] and in this work, the materials are modified by C_2H_2 PIII&D to enhance the properties. Chloride ions exist in seawater, perspiration, and human body fluid and play a critical role in the many corrosion processes. A 0.9 wt% NaCl aqueous solution is a common medium to simulate the human body fluid in corrosion evaluation [33]. In this study, the corrosion behavior of the plasma modified Mg alloy is investigated in a 0.9 wt% sodium chloride solution and the associated mechanism is described.

2. Experimental details

Specimens with dimensions of 10 mm × 10 mm × 5 mm were cut from an extruded Mg–3.0Nd–0.2Zn–0.4Zr (wt%) alloy rod. The microstructure of the materials has been reported [34]. Prior to plasma surface modification, the samples were mechanically ground by up to # 1200 sand papers and ultrasonically cleaned in alcohol. A GPI-100 ion implanter was utilized to conduct plasma immersion ion implantation and deposition (PIII&D). When the base pressure in the vacuum chamber reached about 3×10^{-3} Pa, C_2H_2 gas was introduced at a flow rate of 30 sccm and ionized by a radio frequency (RF) generator with an input power of 1000 W. Short square high-voltage pulses (−20 kV, pulse width of 50 μs, and pulsing frequency of 50 Hz) produced by a pulse modulator were applied to the sample. PIII&D was conducted for 3 h without extra sample heating.

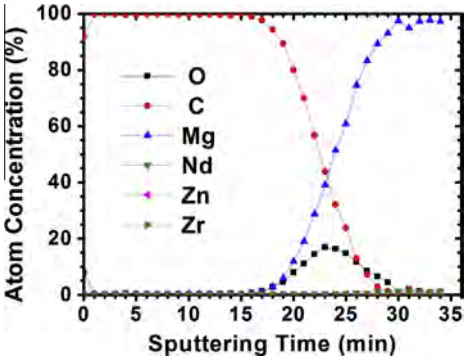

Fig. 2. XPS elemental depth profile of the Mg–Nd–Zn–Zr alloy after PIII&D.

Scanning electron microscopy (SEM) was performed to examine the surface and cross-sectional morphologies and energy dispersive X-ray spectrometry (EDS) was used to determine the elemental composition in the line scan mode. Atomic force microscopy (AFM) was also used to observe the plasma-modified surface. X-ray photoelectron spectroscopy (XPS) with Al Kα irradiation was conducted to acquire elemental depth profiles and determine the chemical states after surface treatment. The sputtering rate was estimated to be about 12 nm min^{-1} based on similar sputtering experiments conducted on a SiO_2 reference. Raman scattering spectra were acquired using a 514.5 nm argon laser (HR LabRAM).

The electrochemical experiments in the 0.9 wt% NaCl solution were carried out on a Zahner Zennium electrochemical workstation based on the three-electrode technique. The potential was referenced to a saturated calomel electrode (SCE) and counter electrode was a platinum sheet. The specimen with a surface area of 10×10 mm^2 was exposed to the NaCl solution and after

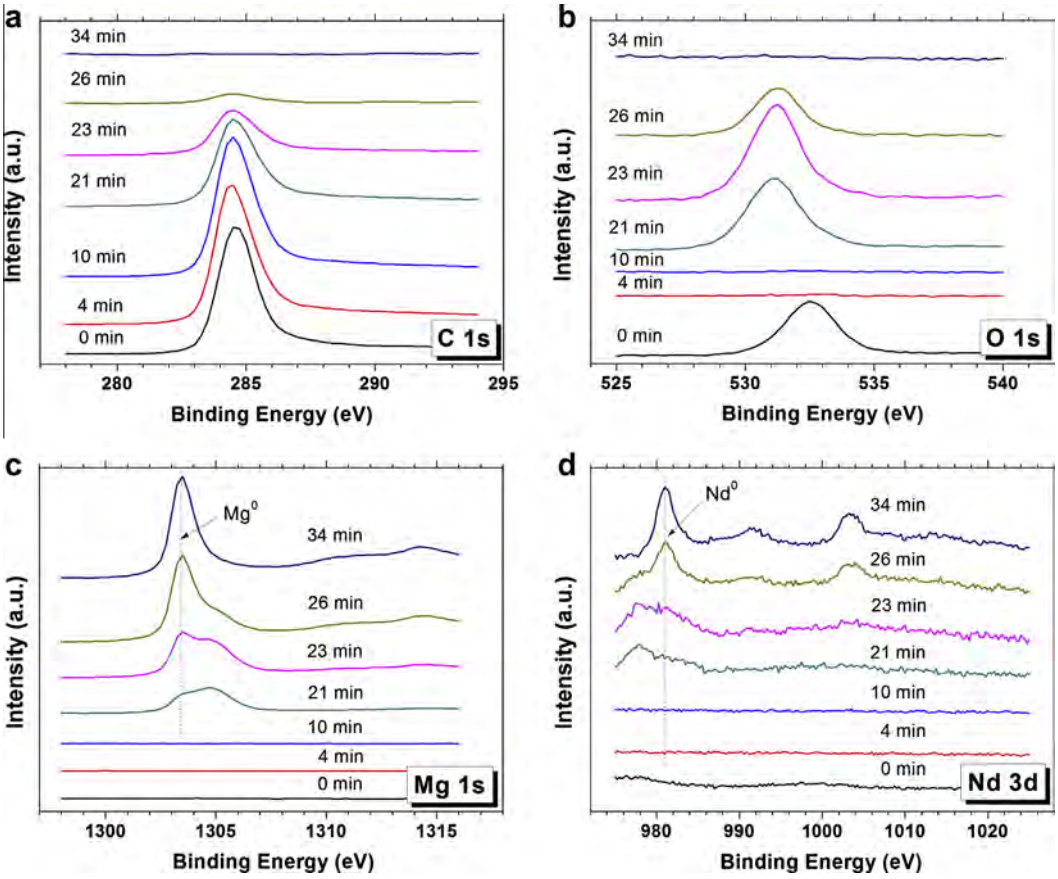

Fig. 3. High-resolution XPS spectra of the treated Mg–Nd–Zn–Zr alloy at different sputtering time: (a) C 1s, (b) O 1s, (c) Mg 1s, and (d) Nd 3d.

immersion for 30 min, the electrochemical impedance spectra (EIS) were collected to investigate the electrode/solution interface. The data were recorded from 100 kHz to 100 mHz with a 5 mV sinusoidal perturbing signal at the open-circuit potential. The potential was scanned from the cathodic region to the anodic region at a rate of 1 mV/s to obtain the polarization curves. An immersion test was also carried out to evaluate the corrosion behavior in the 0.9 wt% NaCl solution. After immersion for 24 h, the surface and cross-sectional morphologies of the corroded samples were observed by SEM in the backscattered electron mode (BSE) and EDS was further used to analyze the corrosion products. In addition, an MTS nanoindenter was used to determine the hardness and elastic modulus using the continuous stiffness measurement (CSM) mode.

3. Results and discussion

PIII&D combines ion implantation and deposition and in the experiments, a pulse modulator is used to produce short and square high-voltage pulses. Within a voltage pulse period (T), ion implantation is conducted during the voltage pulse time (t) and deposition occurs during the rest of the time [35,36]. After plasma treatment for 3 h, the color of the samples changes from silvery white to dark yellow[1] (Fig. 1a). Fig. 1b shows the surface morphology of the plasma-modified Mg–3.0Nd–0.2Zn–0.4Zr (wt%) alloy and Fig. 1c depicts the cross-section of the alloy after plasma modification. A dense film with an average thickness of 198 ± 31 nm is formed on the surface and the EDS line scan in Fig. 1d reveals that it is mainly composed of carbon.

The top layer of the treated sample is further investigated by XPS. Fig. 2 shows three distinct regions: the top part being the carbon film, the bottom being the Mg alloy substrate, and an oxygen-rich region between the film and substrate. It has been shown that an oxide layer is formed after exposure to air or during mechanical polishing [34]. Hence, it is believed that this oxygen peak originates from a surface oxide layer formed before the plasma treatment. Fig. 3 depicts the corresponding high-resolution XPS spectra of C, O, Mg, and Nd. With increasing sputtering time, the C peak intensity decreases (Fig. 3a) and Mg peak intensity increases gradually (Fig. 3c). The O peak is observed at sputtering time of 0 min, 21 min, 23 min, and 26 min (Fig. 3b). The O peak on the surface (corresponding to sputtering time of 0 min) originates from adsorbed oxygen and the oxygen peaks corresponding to sputtering time of 21 min, 23 min, and 26 min suggests an O-rich intermediate region. It is further noted that C peak does not shift significantly with depth even in this O-rich intermediate region. Carbon has smaller electronegativity, thus suggesting a weaker bond with Mg. As shown in Fig. 3c, the oxidized state of Mg is observed from the O-rich intermediate region and the chemical state gradually shifts to the metallic one with depth. Because the standard peak positions of Nd 3d5/2 are 980.8 eV for metallic Nd and 982 eV for Nd_2O_3 [34], Fig. 3d suggests that Nd exists in the metallic state in the inner region and the peak in the O-rich region is attributed to the Auger peak of oxygen (KL23L23, 978 eV [34]).

The Raman scattering spectra acquired from the carbon film in Fig. 4 shows the typical pattern of diamond-like carbon (DLC) [37,38] and can be deconvoluted into two sub-peaks: G band at

[1] For interpretation of color in Fig. 1, the reader is referred to the web version of this article.

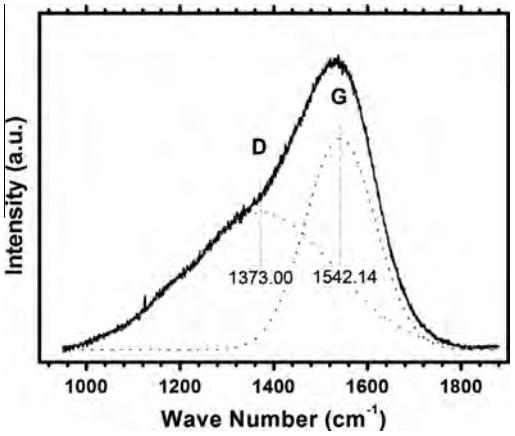

Fig. 4. Raman spectra of the carbon film.

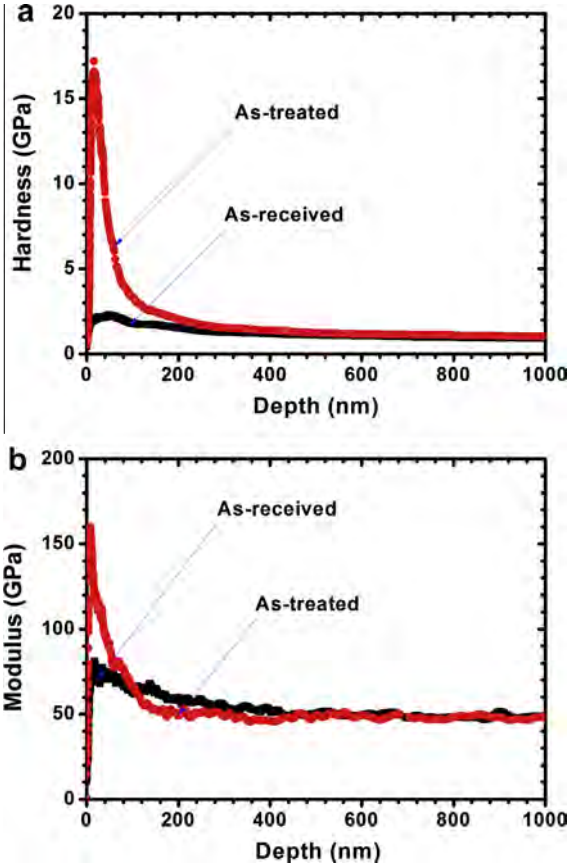

Fig. 5. (a) Hardness and (b) elastic modulus of the samples as a function of displacement.

1542.14 cm^{-1} and D band at 1373.00 cm^{-1}. The G and D bands arise from a graphite structure and disordered graphite-like structure, respectively. In PIII&D, the carbon film is gradually condensed from the plasma containing carbon and hydrocarbon ions. Energetic ion bombardment leads to film growth and induces the formation of sp^3 bonds. Owing to the significant fraction of sp^3 bonds, DLC has high mechanical hardness as well as chemical inertness [39]. Usually, the major drawback is the weak adhesion between DLC and Mg because of the large internal stress resulting from the sp^3 bonds. DLC films prepared by many conventional methods delaminate easily from the Mg substrate [40] but during ion implantation, surface contaminants on the substrate can be removed and energetic ions create radiation damages in the near surface to promote subsequent nucleation. In addition, energetic ion bombardment induces inter-diffusion between the film and substrate [41]. Hence, in PIII&D, adhesion is improved by the above effects synergistically. As shown in Fig. 5a and b, the hardness and elastic modulus of the as-treated sample decrease gradually with indentation depth, finally reaching stable values which represent the hardness and modulus of the bulk substrate. Hence, the surface mechanical properties are significantly improved by the diamond-like carbon thin film.

Electrochemical impedance spectroscopy (EIS) is one of the useful techniques to evaluate the corrosion resistance and analyze the corrosion mechanism. It is almost nondestructive because of a very small perturbing signal applied in the process. The Bode plots including impedance versus frequency and phase angle versus frequency are presented in Fig. 6a and b. Within the range of our investigation, the impedance of the treated sample in any frequency is higher than that of the as-received sample (Fig. 6a). Phase angle evolution is also altered after plasma modification (Fig. 6b). In comparison, there is an extra peak in the higher frequency region overlapping the adjacent peak. In the Nyquist plots (Fig. 6c and d), the capacitive loop of the treated sample is obviously enlarged compared to the untreated sample.

Usually, the capacitive loops are attributed to the surface film, charge transfer, and mass transfer in the corrosion product layer [42]. Here, a constant phase element (CPE) that represents a leaky or non-ideal capacitor replaces the capacitor C based on the Nyquist plots. Its admittance is expressed as follows [43]:

$$Y = Y_0(j\omega)^n \tag{2}$$

where the adjustable parameters Y_0 and n are the admittance constant and empirical exponent, respectively. The as-received and treated samples have different surface states, suggesting different corrosion mechanisms in the NaCl solution. According to the Bode plots and Nyquist plots, the as-received sample has a two-time-constants characteristic and the EIS spectra of the treated sample shows a three-time-constants characteristic within the range of our investigation. The higher frequency region corresponds to the surface film and charge transfer and the lower frequency region is associated with mass transfer [27,34,43]. Song and Xu [44] studied the corrosion behavior of polycrystalline Mg in saturated $Mg(OH)_2$ and 0.01 M NaCl solutions. They suggested that the low frequency capacitive loop was associated with the combination of a pseudo resistance (R) and capacitance related to the film formation and dissolution process (C). Guo et al. [45] prepared a composite film (named as PSPF) on the Mg–Gd–Y alloy and studied the EIS spectra in 3.5 wt% NaCl solution. A parallel combination of the diffusion capacitance (CPE_{diff}) and resistance (R_{diff}) was introduced to describe the "finite-layer diffusion" process or the tangential or heterogeneous penetration of an electrolyte. In this study, an equivalent circuit model with two time constants (outlined in Fig. 6c), $R_s(R_tCPE_{dl})(R_{diff}CPE_{diff})$, is proposed to fit the EIS data of the as-received sample. R_tCPE_{dl} represents the parallel combination of R_t and CPE_{dl}, and $R_{diff}CPE_{diff}$ represents the parallel combination of R_{diff} and CPE_{diff}. R_s is the solution resistance in series with R_tCPE_{dl} and $R_{diff}CPE_{diff}$. CPE_{dl} represents the capacitance of the double layer and R_t is the charge transfer resistance related to the electrochemical reaction. CPE_{diff} represents the capacitance induced by diffusion and R_{diff} is the relevant resistance. As observed from the plasma-treated samples, some of the data in the lower frequency region are scattered. It appears that the inductive loop attributed to the relaxation of adsorbed species such as $Mg(OH)^+_{ads}$ or $Mg(OH)_2$ possibly exists in the lower frequency region. The inductive loop is generally ascribed to pit formation [46,47], but the current data are not sufficient for corroboration. Hence, the equivalent circuit model is

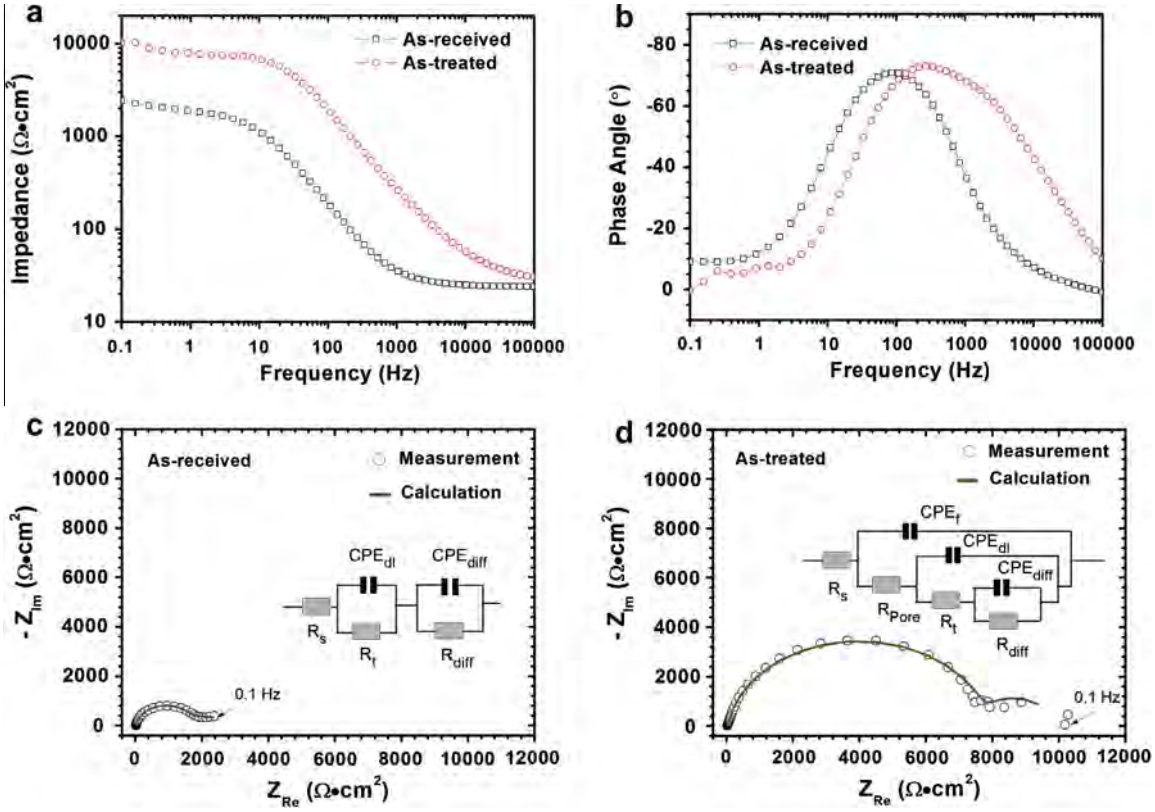

Fig. 6. (a) Bode plots of the as-received and as-treated samples: impedance versus frequency. (b) Bode plots of the as-received and as-treated samples: phase angle versus frequency. (c) Nyquist plots and corresponding equivalent circuit model of the as-received sample. (d) Nyquist plots and corresponding equivalent circuit model of the as-treated sample.

Table 1
Fitted data from the electrochemical impedance spectra (EIS) based on the corresponding equivalent circuit model.

	As-received	As-treated
R_s (Ω cm^2)	25.21 ± 1.651	27.95 ± 2.885
Y_{0f} (Ω^{-2} cm^{-2} s^{-n})		(6.904 ± 1.518) × 10^{-7}
n_f		0.9448 ± 0.03084
R_{pore} (Ω cm^2)		172.5 ± 90.59
Y_{0dl} (Ω^{-2} cm^{-2} s^{-n})	(128.4 ± 2.605) × 10^{-7}	(7.823 ± 1.998) × 10^{-7}
n_{dl}	0.9456 ± 0.008030	0.9163 ± 0.02469
R_t (Ω cm^2)	1104 ± 435.3	5969 ± 1568
Y_{0diff} (Ω^{-2} cm^{-2} s^{-n})	(15.8 ± 7.351) × 10^{-4}	(2.416 ± 2.245) × 10^{-4}
n_{diff}	0.6059 ± 0.0391	0.9808 ± 0.0332
R_{diff} (Ω cm^2)	849.5 ± 267.9	891.8 ± 861.3

simplified as follows: $R_s(CPE_f(R_{pore}(CPE_{dl}(R_t(CPE_{diff}R_{diff})))))$. Here, R_s represents the solution resistance, CPE_{dl} represents the capacitance of the double layer, and R_t is the charge transfer resistance related to the electron transfer in the faradic process. CPE_{diff} also represents the capacitance pertaining to the diffusion and R_{diff} thus represents the relevant resistance. In addition, CPE_f denotes the capacitance of the deposited film and R_{pore} is the total resistance of the pores in the film. The fitted data are shown in Table 1. Because R_s is small and similar in all the tests, it is neglected here. R_p, the sum of R_t and R_{diff} or the sum of R_{pore}, R_t and R_{diff}, is proposed to evaluate the corrosion resistance. Obviously, R_p representing the polarization resistance becomes higher after the surface treatment, implying that the corrosion resistance in the NaCl solution is improved.

Fig. 7a displays the polarization curves acquired in the NaCl solution. Generally, the anodic region describes dissolution of the sample under an elevated potential and the cathodic polarization curve represents cathodic hydrogen evolution *via* the water reduction reaction. The as-received sample exhibits a two-regime anodic polarization behavior. The dissolution rate abruptly turns from slow to rapid as the potential is raised to a certain value in the anodic region. In comparison, the curve of the plasma-treated sample shifts to higher potential and lower current density. Moreover, it shows a simple activation-controlled anodic behavior. The corrosion behavior of the DLC-coated alloy is suggested to be controlled by the exposed substrate in the solution. When the applied potential exceeds the corrosion potential, the exposed substrate is vulnerable to pitting corrosion because the substrate is already in the active anodic region referenced to its own polarization curve. The corrosion potential and corrosion current density are often applied to evaluate the corrosion resistance and they can be derived by Tafel extrapolation from the linear cathodic polarization region. The results are shown in Fig. 7b and c. After plasma modification, the corrosion potential is improved and the corrosion current density is significantly reduced, suggesting that the plasma-modified samples have better corrosion resistance in the NaCl solution.

Immersion tests are carried out to investigate the corrosion behavior of the treated Mg alloy in the 0.9 wt% NaCl solution. Before immersion, the surface appearance of the as-received and plasma-treated samples is examined by SEM. As shown in Fig. 8a, the second phase, $Mg_{12}Nd$, is observed from the surface of the as-received sample (ground by # 1200 sand paper) and it is in agreement with the metallographic analysis reported in the literature [31,32,34]. In spite of the thin film covering the surface after surface modification, the second phase can still be identified (Fig. 8b). It is further observed that some defects with a size of about 10 μm are randomly distributed on the surface and one of

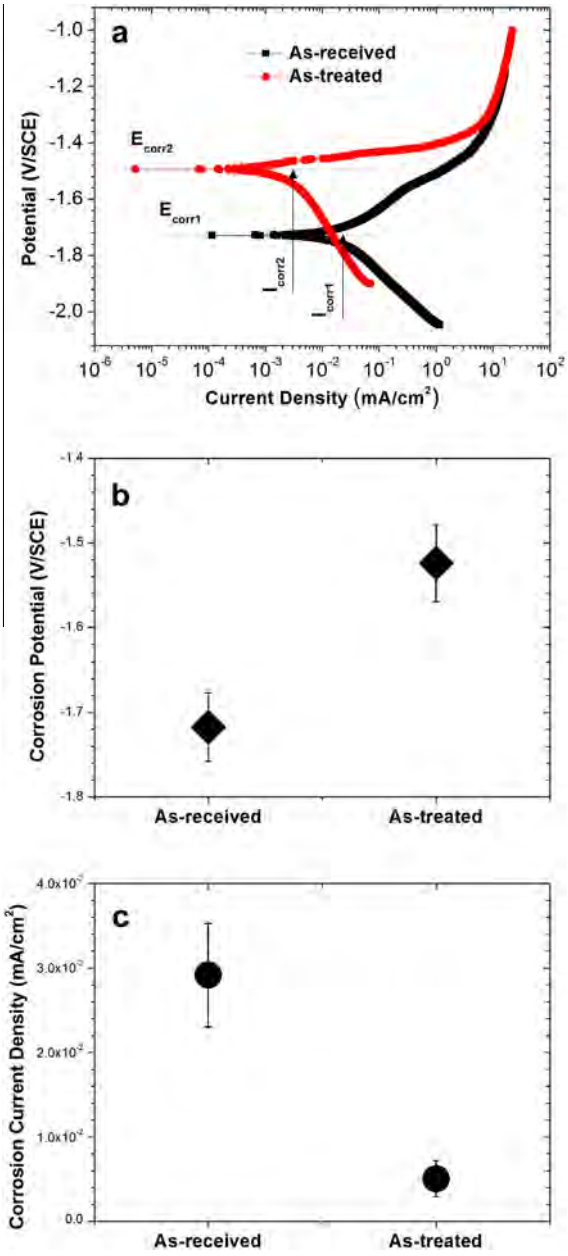

Fig. 7. (a) Polarization curves of the as-received and as-treated samples. (b) Corrosion potential obtained from the polarization curve *via* cathodic Tafel fitting. (c) Corrosion current density obtained from the polarization curve by cathodic Tafel fitting.We revised this figure, and new one is attached. In Fig. 7b, corrosion potential (V) –> corrosion potential (V/SCE).

them is depicted in Fig. 8c. Based on the aforementioned analysis, a schematic is proposed to describe the film structure (Fig. 8d). Generally, the structure of vapor deposited coatings consists typically of a columnar growth structure. If the deposited atoms have insufficient energy, voided growth defects will be formed easily due to atomic shadowing. In particular, when a significant oblique component emerges in the coating flux, shadowing will induce open boundaries because high points on the growing surface receive more coating flux than valleys [25]. Here, the columnar structure does not form during PIII&D because of energetic ion bombardment. Consequently, most of the surface is covered by a continuous film but other factors such as dirt and sparkle lead to some discontinuous regions which have poorer protective effects.

After immersion for 24 h, the as-received sample suffers from corrosion as shown in Fig. 9a–f. In order to better describe the phenomenon, the corroded surface is divided into two parts: a slightly-corroded region and another severely corroded region (Fig. 9a). Fig. 9b and c shows the web-like morphology of the slightly-corroded region, providing evidence of corrosion products. The more severe corrosion is presented with gradual magnification in Fig. 9d–f which discloses the hierarchical characteristics in longitudinal propagation. Fig. 10a–f shows the surface morphology of the as-treated Mg alloy after immersion. Obviously, only a part of the surface suffers from corrosion (Fig. 10a) and in the un-corroded region, the surface is intact (Fig. 10b and c). Similar to the pictures acquired before immersion, second phases can be identified here. Fig. 10e shows a platelet-like surface film on the surface which is similar to that reported before [48]. Fig. 10f acquired from another site clearly describes the contours of the corrosion pit consisting of the Mg substrate, DLC film, and surface film.

Fig. 11a and b presents the cross section of the untreated Mg–3.0Nd–0.2Zn–0.4Zr (wt%) alloy after immersion for 24 h showing a layer of corrosion products on the surface. The thicknesses at different sites are different and it is corroborated by Fig. 9. EDS reveals that the products are mainly composed of Mg and O and EDS mapping further identifies the corrosion product and substrate clearly. Chang et al. [47] immersed Mg–3.0Nd–0.2Zn–0.4Zr (wt%) alloy in a 5 wt% NaCl solution for 216 h and confirmed that the corrosion product was mainly composed of $Mg(OH)_2$ by means of XRD. Fig. 11c and d shows the cross section of the plasma-treated sample after immersion. Fig. 11c presents the view of the uncorroded region and one of the insets shows the magnified view confirming existence of the DLC film after immersion. In comparison, corrosion of the substrate in the pits is evident as shown in Fig. 11d. EDS mapping is also an effective tool to describe the corrosion of magnesium alloy and with the DLC film, most of the surface region is protected in the aggressive NaCl solution.

According to the electrochemical and immersion tests, the corrosion resistance of Mg–Nd–Zn–Zr alloy is improved after the plasma treatment. Diamond-like carbon (DLC) is quite anticorrosive in nature [39] and the DLC film formed in this study is also very dense from the perspective of intrinsic microstructure (Fig. 1) despite some random defects on the surface (Fig. 8c). Those defects possibly stem from the treatment process or originally defective surface. With the DLC film, the polarization resistance of the cathode ($R_{p(C)}$) and electrical resistance between the anode and cathode ($R_{Mg\text{-}C}$) are quite high and so the galvanic effect is weakened. The immersion test also shows that these defects become shortcuts for aggressive media to enter the coating/substrate system and corrosive attack commences when the media arrive at the coating/substrate interface. XPS (Fig. 2) reveals the existence of an oxide layer on the Mg substrate. Generally speaking, the native surface oxide film formed during exposure to air consists of mainly MgO. According to thermodynamics, MgO is not stable in an aqueous solution and will be converted into magnesium hydroxide. OH^- is replaced by Cl^- to form chloride which expedites dissolution of the surface structure [34]. On the newly exposed magnesium, the overall corrosion reaction can be described as follows: $Mg + 2H_2O \rightarrow Mg^{2+} + 2OH^- + H_2\uparrow$ [49]. Dissolution of Mg increases the OH^- concentration near the sites around the defects. When the solubility limit is exceeded, $Mg(OH)_2$ will precipitate [50,51] and the platelet-like film in the corroded region (Fig. 10e) can be attributed to this dissolution-precipitation mechanism. Accompanying the damage of the substrate, the pits propagate gradually finally leading to failure of the coating. In summary, PIII&D with C_2H_2 as gas source provides a new way to improve the surface corrosion resistance of Mg alloys. With further process optimization, its application is expected to broaden. For instance, PIII&D can constitute a pre-treatment process prior to coating deposition or other surface modification.

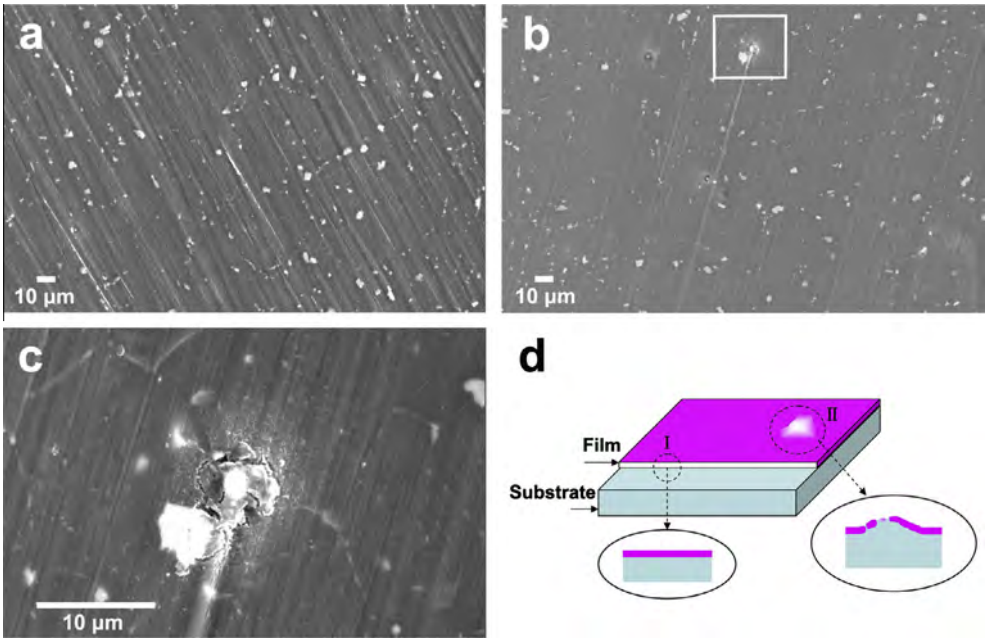

Fig. 8. (a) Surface morphology of the as-received sample after grinding. (b) Surface morphology of the as-treated sample. (c) Magnified surface defect on the as-treated sample corresponding to the rectangular box in panel (b). (d) Schematic of the film structure with random defects.

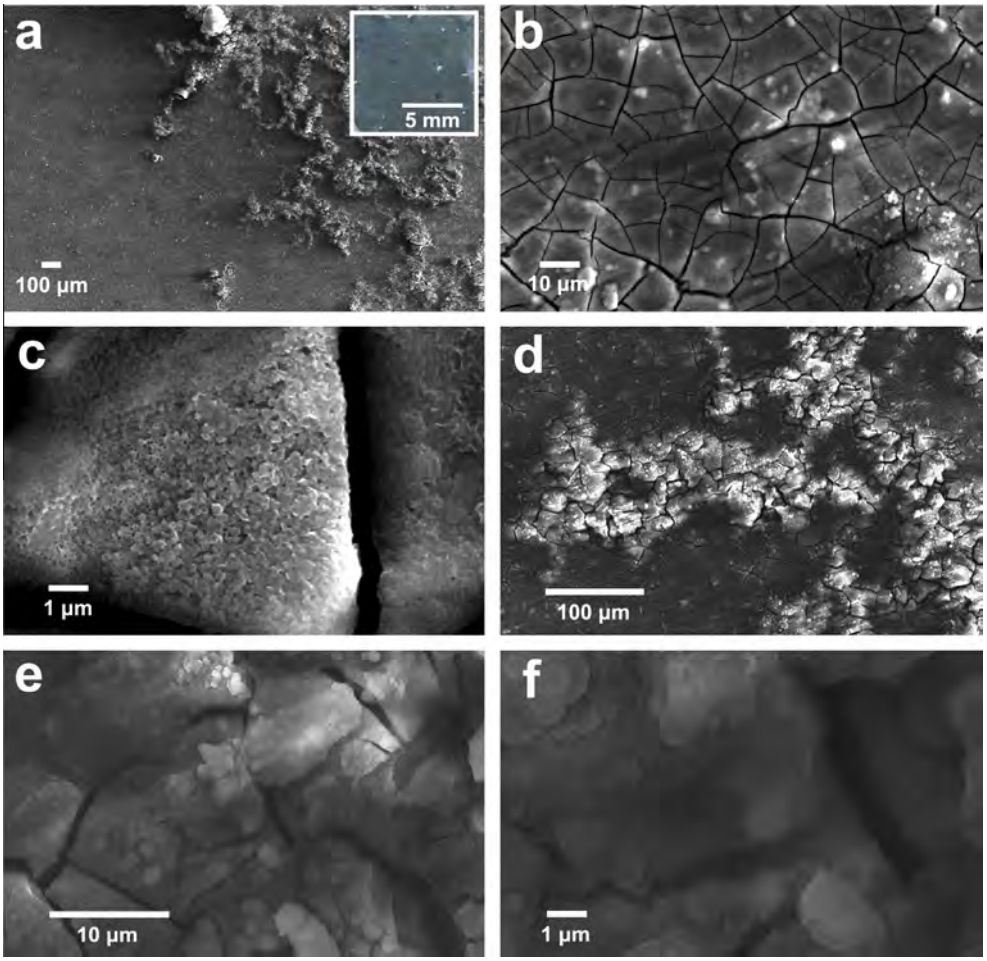

Fig. 9. (a) Surface morphology of the as-received sample after immersion in the 0.9 wt% NaCl solution for 24 h with the inset showing the overall view captured by a digital camera. (b and c) Surface morphology of the slightly-corroded region with panel (c) showing a magnified view. (d–f) Surface morphology of the severely-corroded region with panels (e) and (f) showing the magnified region step by step.

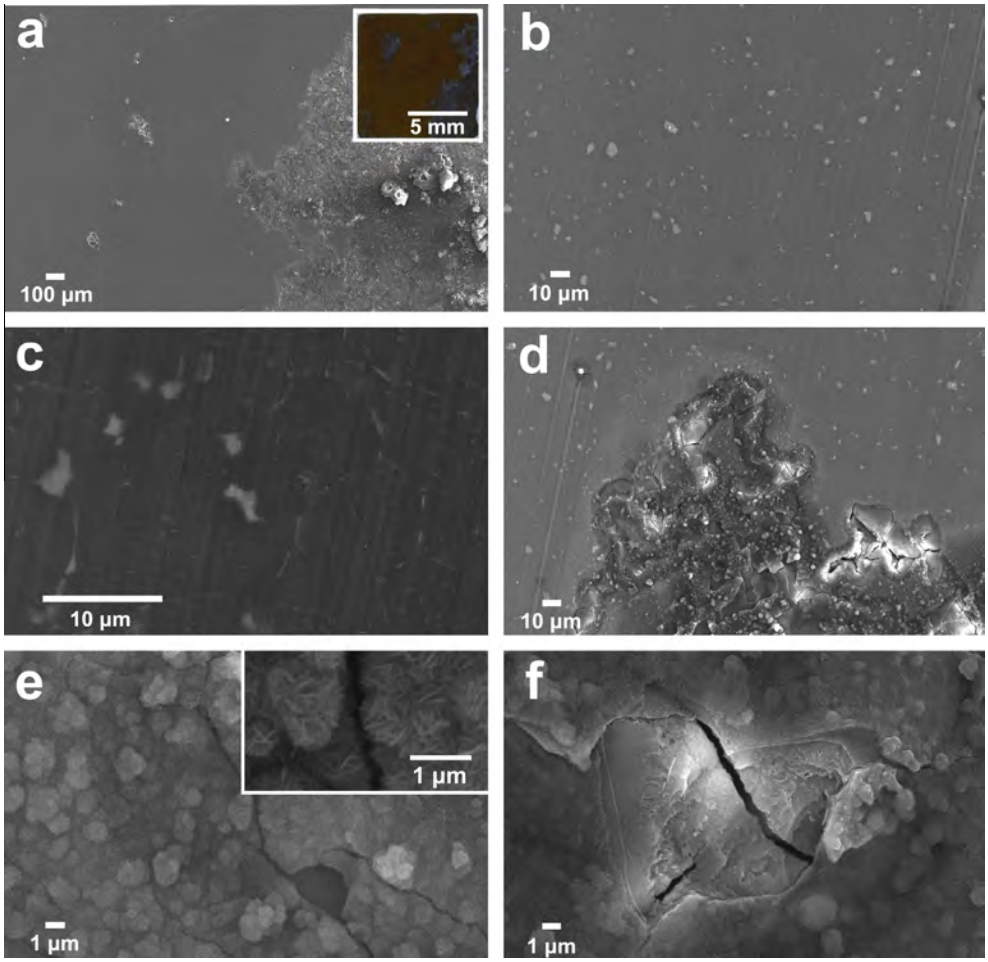

Fig. 10. (a) Surface morphology of the as-treated sample after immersion in the 0.9 wt% NaCl solution for 24 h with the inset showing the overall view captured by a digital camera. (b and c) Surface morphology of the un-corroded region with panel (c) showing a magnified view. (d–f) Surface morphology of the corroded region with panels (e) and (f) showing the two different magnified regions and the inset in panel (e) showing the magnified surface film formed on the carbon film.

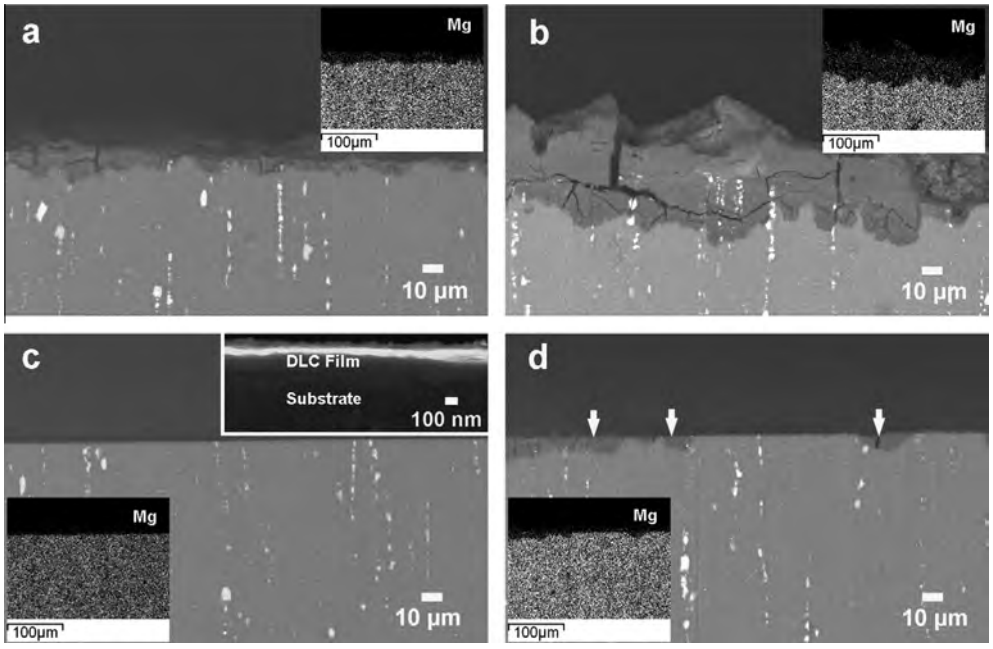

Fig. 11. Cross sections of the corroded samples at different sites: (a and b) as-received sample and (c and d) as-treated sample. The EDS map of Mg is shown in each panel as an inset. One of the insets in panel (c) shows the remnant carbon film at high magnification. The arrows in panel (d) indicate the corrosion pits.

4. Conclusion

Mg–Nd–Zn–Zr alloy is modified by C_2H_2 plasma immersion ion implantation and deposition (PIII&D). After the plasma treatment, a thin diamond-like carbon film is formed on the surface of Mg–Nd–Zn–Zr alloy. Both electrochemical and immersion tests reveal enhanced corrosion resistance in the 0.9 wt% NaCl solution. The improvement is attributed to the good barrier effect of the diamond-like carbon film but random defects in the film induce corrosion failure of the plasma-modified Mg–Nd–Zn–Zr alloy eventually.

Acknowledgments

This work was financially supported by Hong Kong Research Grants Council (RGC) General Research Funds (GRF) Nos. CityU 112510 and 112212, City University of Hong Kong Applied Research Grant (ARG) No. 9667066, and National Nature Science Foundation of China No. 51174136. The authors thank Dr. Ricky K. Fu (Plasma Technology Ltd., Hong Kong) for helpful discussions.

References

[1] B.L. Mordike, T. Ebert, Magnesium: properties-applications-potential, Mater. Sci. Eng. A 302 (2001) 37–45.
[2] S.R. Agnew, J.F. Nie, Preface to the viewpoint set on: the current state of magnesium alloy science and technology, Scripta Mater. 63 (2010) 671–673.
[3] Y. Lu, Q. Wang, X. Zeng, W. Ding, C. Zhai, Y. Zhu, Effects of rare earths on the microstructure, properties and fracture behavior of Mg–Al alloys, Mater. Sci. Eng. A 278 (2000) 66–76.
[4] C. Ma, M. Liu, G. Wu, W. Ding, Y. Zhu, Tensile properties of extruded ZK60-RE alloys, Mater. Sci. Eng. A 349 (2003) 207–212.
[5] G. Song, Control of biodegradation of biocompatible magnesium alloys, Corros. Sci. 49 (2007) 1696–1701.
[6] M.P. Staiger, A.M. Pietak, J. Huadmai, G. Dias, Magnesium and its alloys as orthopedic biomaterials: a review, Biomaterials 27 (2006) 1728–1734.
[7] H. Friedrich, S. Schumann, Research for a "new age of magnesium" in the automotive industry, J. Mater. Process. Technol. 117 (2001) 276–281.
[8] G. Song, M. Liu, The effect of Mg alloy substrate on "electroless" E-coating performance, Corros. Sci. 53 (2011) 3500–3508.
[9] G. Song, M. Liu, The effect of surface pretreatment on the corrosion performance of electroless E-coating coated AZ31, Corros. Sci. 62 (2012) 61–72.
[10] J. Hu, D. Huang, G. Zhang, G. Song, X. Guo, Research on the inhibition mechanism of tetraphenylporphyrin on AZ91D magnesium alloy, Corros. Sci. 63 (2012) 367–378.
[11] J. Uan, S. Yu, M. Lin, L. Chen, H. Lin, Evolution of hydrogen from magnesium alloy scraps in citric acid-added seawater without catalyst, Int. J. Hydrogen Energy 34 (2009) 6137–6142.
[12] B. Yu, J. Uan, Sacrificial Mg film anode for cathodic protection of die cast Mg–9 wt%Al–1 wt%Zn alloy in NaCl aqueous solution, Scripta Mater. 54 (2006) 1253–1257.
[13] F. Witte, V. Kaese, H. Haferkamp, E. Switzer, A. Meyer-Lindenberg, C.J. Wirth, H. Windhagen, In vivo corrosion of four magnesium alloys and the associated bone response, Biomaterials 26 (2005) 3557–3563.
[14] B. Zberg, P.J. Uggowitzer, J.F. Löffler, MgZnCa glasses without clinically observable hydrogen evolution for biodegradable implants, Nat. Mater. 8 (2009) 887–891.
[15] Y. Zhao, G. Wu, J. Jiang, H.M. Wong, K.W.K. Yeung, P.K. Chu, Improved corrosion resistance and cytocompatibility of magnesium alloy by two-stage cooling in thermal treatment, Corros. Sci. 59 (2012) 360–365.
[16] L. Wang, Y. Gao, H. Liu, Q. Xue, T. Xu, Effects of bivalent Co ion on the co-deposition of nickel and nano-diamond particles, Surf. Coat. Technol. 191 (2005) 1–6.
[17] Z. Zeng, L. Wang, L. Chen, J. Zhang, The correlation between the hardness and tribological behaviour of electroplated chromium coatings sliding against ceramic and steel counterparts, Surf. Coat. Technol. 201 (2006) 2282–2288.
[18] Z. Shi, G. Song, A. Atrens, The corrosion performance of anodized magnesium alloys, Corros. Sci. 48 (2006) 3531–3546.
[19] J. Liang, P.B. Srinivasan, C. Blawert, W. Dietzel, Comparison of electrochemical corrosion behaviour of MgO and ZrO_2 coatings on AM50 magnesium alloy formed by plasma electrolytic oxidation, Corros. Sci. 51 (2009) 2483–2492.
[20] S. Mao, H. Yang, Z. Song, J. Li, H. Ying, K. Sun, Corrosion behaviour of sintered NdFeB deposited with an aluminium coating, Corros. Sci. 53 (2011) 1887–1894.
[21] X. Liu, P.K. Chu, C. Ding, Surface modification of titanium, titanium alloys, and related materials for biomedical applications, Mater. Sci. Eng. R 47 (2004) 49–121.
[22] G. Song, B. Johannesson, S. Hapugoda, D. StJohn, Galvanic corrosion of magnesium alloy AZ91D in contact with an aluminium alloy, steel and zinc, Corros. Sci. 46 (2004) 955–977.
[23] M. Finsgar, Galvanic series of different stainless steels and copper- and aluminium-based materials in acid solutions, Corros. Sci. 68 (2013) 51–56.
[24] H. Hoche, C. Rosenkranz, A. Delp, M.M. Lohrengel, E. Broszeit, C. Berger, Investigation of the macroscopic and microscopic electrochemical corrosion behaviour of PVD-coated magnesium die cast alloy AZ91, Surf. Coat. Technol. 193 (2005) 178–184.
[25] G. Wu, W. Dai, H. Zheng, A. Wang, Improving wear resistance and corrosion resistance of AZ31 magnesium alloy by DLC/AlN/Al coating, Surf. Coat. Technol. 205 (2010) 2067–2073.
[26] G. Wu, L. Sun, W. Dai, L. Song, A. Wang, Influence of interlayers on corrosion resistance of diamond-like carbon coating on magnesium alloy, Surf. Coat. Technol. 204 (2010) 2193–2196.
[27] G. Wu, A. Shanaghi, Y. Zhao, X. Zhang, R. Xu, Z. Wu, G. Li, P.K. Chu, The effect of interlayer on corrosion resistance of ceramic coating/Mg alloy substrate in simulated physiological environment, Surf. Coat. Technol. 206 (2012) 4892–4898.
[28] Y. Liu, L. Li, X. Cai, Q. Chen, M. Xu, Y. Hu, T. Cheung, C.H. Shek, P.K. Chu, Effects of pretreatment by ion implantation and interlayer on adhesion between aluminum substrate and TiN film, Thin Solid Films 493 (2005) 152–159.
[29] G. Wu, K. Ding, X. Zeng, X. Wang, S. Yao, Improving corrosion resistance of titanium-coated magnesium alloy by modifying surface characteristics of magnesium alloy prior to titanium coating deposition, Scripta Mater. 61 (2009) 269–272.
[30] G. Wu, J.M. Ibrahim, P.K. Chu, Surface design of biodegradable magnesium alloys – a review, Surf. Coat. Technol. 233 (2013) 2–12.
[31] F. Penghuai, P. Liming, J. Haiyan, C. Jianwei, Z. Chunquan, Effects of heat treatments on the microstructures and mechanical properties of Mg–3Nd–0.2Zn–0.4Zr (wt%) alloy, Mater. Sci. Eng. A 486 (2008) 183–192.
[32] X. Zhang, G. Yuan, L. Mao, J. Niu, P. Fu, W. Ding, Effects of extrusion and heat treatment on the mechanical properties and biocorrosion behaviors of a Mg–Nd–Zn–Zr alloy, J. Mech. Behav. Biomed. Mater. 7 (2012) 77–86.
[33] C.L. Liu, Y.J. Wang, R.C. Zeng, X.M. Zhang, W.J. Huang, P.K. Chu, *In vitro* corrosion degradation behaviour of Mg–Ca alloy in the presence of albumin, Corros. Sci. 52 (2010) 3341–3347.
[34] G. Wu, K. Feng, A. Shanaghi, Y. Zhao, R. Xu, G. Yuan, P.K. Chu, Effects of surface alloying on electrochemical corrosion behavior of oxygen-plasma-modified biomedical magnesium alloy, Surf. Coat. Technol. 206 (2012) 3186–3195.
[35] R.K.Y. Fu, P.K. Chu, X. Tian, Influence of thickness and dielectric properties on implantation efficacy in plasma immersion ion implantation of insulators, J. Appl. Phys. 95 (2004) 3319–3323.
[36] Y. Huang, S. Lv, X. Tian, R.K.Y. Fu, P.K. Chu, Interface analysis of inorganic films on polyimide with atomic oxygen exposure, Surf. Coat. Technol. 216 (2013) 121–126.
[37] P.K. Chu, L. Li, Characterization of amorphous and nanocrystalline carbon films, Mater. Chem. Phys. 96 (2006) 253–277.
[38] N. Yamauchi, N. Ueda, A. Okamoto, T. Sone, M. Tsujikawa, S. Oki, DLC coating on Mg–Li alloy, Surf. Coat. Technol. 201 (2007) 4913–4918.
[39] J. Robertson, Diamond-like amorphous carbon, Mater. Sci. Eng. R 37 (2002) 129–281.
[40] W. Dai, G. Wu, A. Wang, Preparation, characterization and properties of Cr-incorporated DLC films on magnesium alloy, Diamond Relat. Mater. 19 (2010) 1307–1315.
[41] Y. Liu, L. Li, M. Xu, Q. Chen, Y. Hu, X. Cai, P.K. Chu, The effect of N^+-implanted aluminum substrate on the mechanical properties of TiN films, Surf. Coat. Technol. 200 (2006) 2672–2678.
[42] Y. Xin, T. Hu, P.K. Chu, Degradation behaviour of pure magnesium in simulated body fluids with different concentrations of HCO_3^-, Corros. Sci. 53 (2011) 1522–1528.
[43] C. Liu, Q. Bi, A. Leyland, A. Matthews, An electrochemical impedance spectroscopy study of the corrosion behaviour of PVD coated steels in 0.5 N NaCl aqueous solution: Part I. Establishment of equivalent circuits for EIS data modelling, Corros. Sci. 45 (2003) 1243–1256.
[44] G. Song, Z. Xu, Crystal orientation and electrochemical corrosion of polycrystalline Mg, Corros. Sci. 63 (2012) 100–112.
[45] X. Guo, K. Du, Q. Guo, Y. Wang, R. Wang, F. Wang, Effect of phytic acid on the corrosion inhibition of composite film coated on Mg–Gd–Y alloy, Corros. Sci. 76 (2013) 129–141.
[46] M. Jamesh, S. Kumar, T.S.N.S. Narayanan, Corrosion behavior of commercially pure Mg and ZM21 Mg alloy in Ringer's solution – long term evaluation by EIS, Corros. Sci. 53 (2011) 645–654.
[47] J. Chang, X. Guo, P. Fu, L. Peng, W. Ding, Effect of heat treatment on corrosion and electrochemical behaviour of Mg–3Nd–0.2Zn–0.4Zr (wt%) alloy, Electrochim. Acta 52 (2007) 3160–3167.
[48] G. Wu, X. Zeng, S. Yao, X. Wang, Formation of a novel nanocrystalline coating on AZ31 magnesium alloy by bias sputtering, Mater. Lett. 61 (2007) 4019–4022.
[49] Y. Song, D. Shan, R. Chen, F. Zhang, E. Han, Formation mechanism of phosphate conversion film on Mg–8.8Li alloy, Corros. Sci. 51 (2009) 62–69.
[50] G. Wu, Y. Zhao, X. Zhang, J.M. Ibrahim, P.K. Chu, Self-protection against corrosion of aged magnesium alloy in simulated physiological environment, Corros. Sci. 68 (2013) 279–285.
[51] M. Taheri, R.C. Phillips, J.R. Kish, G.A. Botton, Analysis of the surface film formed on Mg by exposure to water using a FIB cross-section and STEM–EDS, Corros. Sci. 59 (2012) 222–228.